Self-Assembly of Protein Nanofibrils Orchestrates Calcite Step Movement through Selective Nonchiral Interactions

Christopher R. So,[†,⊥] Jinny Liu,[‡] Kenan P. Fears,[†] Dagmar H. Leary,[‡] Joel P. Golden,[‡] and Kathryn J. Wahl*[,†]

[†]Chemistry Division, US Naval Research Laboratory, 4555 Overlook Avenue SW, Washington, DC 20375, United States and [‡]Center for Bio/Molecular Science and Engineering, US Naval Research Laboratory, 4555 Overlook Avenue SW, Washington, DC 20375, United States. [⊥]National Research Council Post-Doctoral Fellow

ABSTRACT The recognition of atomically distinct surface features by adsorbed biomolecules is central to the formation of surface-templated peptide or protein nanostructures. On mineral surfaces such as calcite, biomolecular recognition of, and self-assembly on, distinct atomic kinks and steps could additionally orchestrate changes to the overall shape and symmetry of a bulk crystal. In this work, we show through *in situ* atomic force microscopy (AFM) experiments that an acidic 20 kDa cement protein from the barnacle *Megabalanus rosa* (MRCP20) binds specifically to step edge atoms on $\{10\bar{1}4\}$ calcite surfaces, remains bound and further assembles over time to form one-dimensional nanofibrils. Protein nanofibrils are continuous and organized at the nanoscale, exhibiting striations with a period of ca. 45 nm. These fibrils, templated by surface steps of a preferred geometry, in turn selectively dissolve underlying calcite features displaying the same atomic arrangement. To demonstrate this, we expose the protein solution to bare and fibril-associated rhombohedral etch pits to reveal that nanofibrils accelerate only the movement of fibril-forming steps when compared to undecorated steps exposed to the same solution conditions. Calcite mineralized in the presence of MRCP20 results in asymmetric crystals defined by frustrated faces with shared mirror symmetry, suggesting a similar step-selective behavior by MRCP20 in crystal growth. As shown here, selective surface interactions with step edge atoms lead to a cooperative regime of calcite modification, where templated long-range protein nanostructures shape crystals.

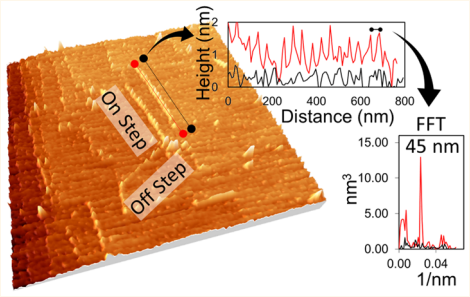

KEYWORDS: molecular self-assembly · proteins · atomic force microscopy · calcite · adsorption · nanofibril

Self-assembled biomolecular nanostructures play an important and well-established role in orchestrating the nucleation and growth of crystalline materials in complex mineral composites such as teeth and bone.[1−5] As an alternative formation mechanism, surface-aligned protein and peptide nanostructures have been directly formed on and templated by inorganic crystals that exhibit weakly attractive, noncovalent chemistries.[6−8] In general, biological nanomaterials can be formed by surfaces that share two common attributes: distinct features that can be chemically recognized and atomically flat lattices that propagate the growth of structures in the nano- to micrometer length scale. For example, molecular interactions with distinct lattice arrangements on inorganic surfaces such as gold, graphite, and mica have led to the formation of peptide or protein nanostructures that are aligned to the symmetry of surface atoms.[9,10] Minerals such as calcite have ideal surface properties to form aligned biomolecular assemblies, with atomically flat terraces that are defined by raised steps of distinct chirality or spatial arrangement.[11−13] Though self-assembly has been investigated on inert materials, little is known about whether proteins assemble and cooperate on mineral surfaces such as calcite.

Proteinaceous secretions from the barnacle *Amphibalanus amphitrite* (*Balanus amphitrite*) have been found to exist largely as microns-long nanofibrils that exhibit β-pleated sheet content similar to amyloid protein assemblies.[14,15] Such long-range biomolecular nanostructures secreted by barnacles may function differently from cementing or shell-forming proteins found

* Address correspondence to kathryn.wahl@nrl.navy.mil.

Received for review January 9, 2015 and accepted May 13, 2015.

Published online May 13, 2015
10.1021/acsnano.5b01870

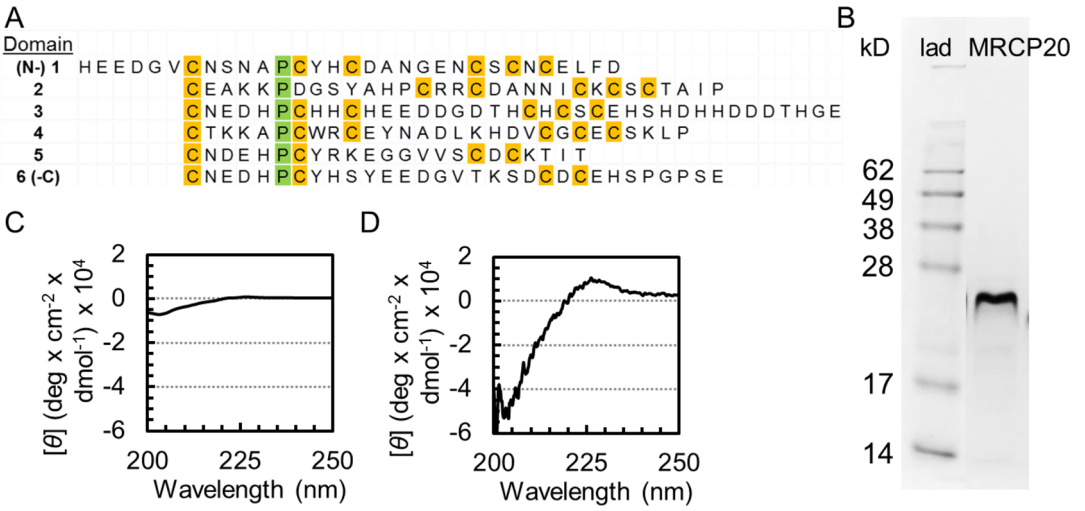

Figure 1. (A) Primary protein sequence of MRCP20 aligned by shared cysteine and proline positions into six domains. (B) SDS-PAGE of purified recombinant MRCP20. Circular dichroism spectrum of MRCP20 mean residue molar ellipticity (C) before and (D) after removal of β-ME by solvent exchange.

in other sessile organisms, as interactions occur through a networked cohesive glue.[13,16,17] For example, barnacle adhesive proteins play a dual role in adhering to both the native organism carbonate shell and a foreign substratum, which is often exposed crystalline calcium carbonate from other marine invertebrates or sedimentary minerals. The necessary cohesion of barnacle cement suggests that adhesive proteins may employ long-range assembly strategies to manipulate, and adhere to, such commonly encountered materials.

Of particular interest has been an acidic 20 kD protein isolated from the primary cement of *M. rosa* (MRCP20) that maintains a β turn and random coil secondary structure in solution.[18] Although this protein is thought capable of assembling into long-range fibrils in solution, it has only been demonstrated using a 24-residue peptide fragment generated from one of six homologous domains in the primary sequence.[19] The 20 kDa protein has an isoelectric point of 4.7 and is composed primarily of cysteine (17%), aspartic acid (11.5%), glutamic acid (10.4%), and histidine (10.4%) as seen in Figure 1A.[18,20] An abundance of acidic residues sets MRCP20 apart from the composition of other major proteins found to date in barnacle cement. While the cysteine residues have been identified as structural,[18] the abundance of both Asp/Glu and His suggests that this protein may purposefully interact with free ionic species or solid mineral surfaces. Mori *et al.* have demonstrated this protein to exhibit affinity toward calcite in both DI water and artificial seawater, with micromolar affinity.[18] Transcriptome analysis using cDNA and RNA from *A. amphitrite* and *Fistulobalanus albicostatus* has identified homologous proteins in both organisms with shared cysteine motifs and charged residue composition, further verified in *A. amphitrite* to be localized in the base plate region of the barnacle.[18,21] Binding assays involving MRCP20 and various solid surfaces have indicated this protein displays a significant affinity for calcite over other materials found in marine environments.[18] However, as calcite growth and dissolution in water are determined by the movement of raised atomic surface features, the mechanism of MRCP20 interaction with mineral surfaces has yet to be explored.

In this work, we aim to understand the molecular mechanism of MRCP20 interaction with calcite and how templated higher ordered protein structures affect calcite surface features. We have recombinantly expressed a soluble form of MRCP20 in *E. coli* and confirmed that it maintains a similar secondary structure to previous recombinant forms as well as the wild-type isolated from *M. rosa* barnacles. To study soft protein assemblages, intermittent contact mode AFM (ICM-AFM) experiments are carried out on calcite, where the formation of long protein nanofibrils is observed on high energy steps with shared orientation. The existence of striated off-edge fibril segments confirms that observed protein structures are continuous. Separately, *in situ* contact-mode AFM (CM-AFM) of etch pit growth directly monitors how known atomic surface features are affected by proteins in bulk or fibril form. Fibrils are observed to be highly selective, displaying a 5-fold preference for obtuse steps over acute steps of rhombohedral etch pits on the $\{10\bar{1}4\}$ face, a 2-fold enhancement over interactions with bulk solution proteins. This selectivity plays a role in mineralization experiments where asymmetric calcite crystals form under supersaturated conditions in the presence of MRCP20, demonstrating the effect of cooperative protein interactions in shaping calcite.

RESULTS

Expression of Recombinant MRCP20. To obtain tag-free MRCP20, His-tagged protein was purified and cleaved

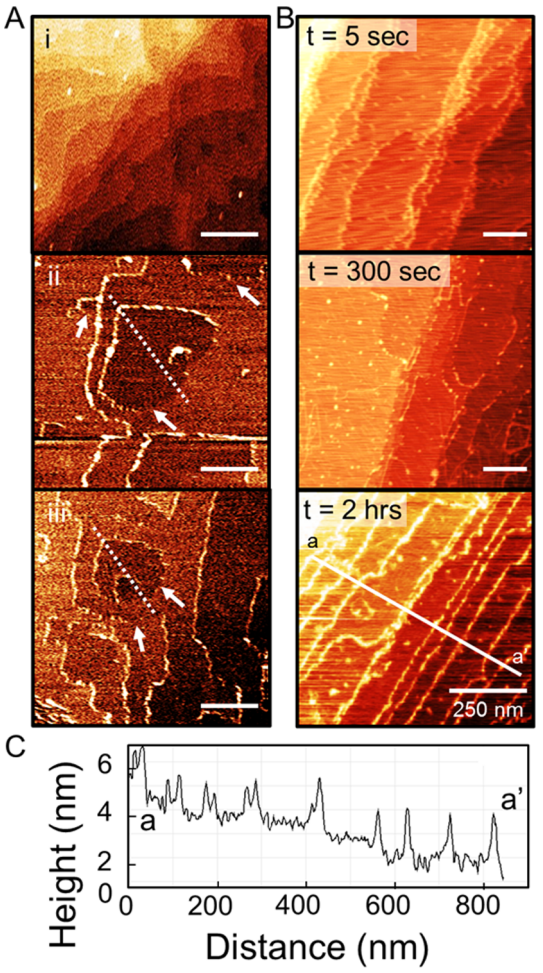

Figure 2. (A) Representative *in situ* AFM images of MRCP20 nanofibrils templated by specific steps: (i) bare calcite; (ii, iii) two images showing calcite etch pits selectively decorated with MRCP20. Dotted lines represent glide plane symmetry, and white arrows point to nondecorated steps. (B) Time-lapse *ex situ* AFM of nanofibril formation by MRCP20 on calcite steps after 5, 300, and 7200 s exposure to protein. (C) Representative cross-section of edge-decorated steps showing fibril heights.

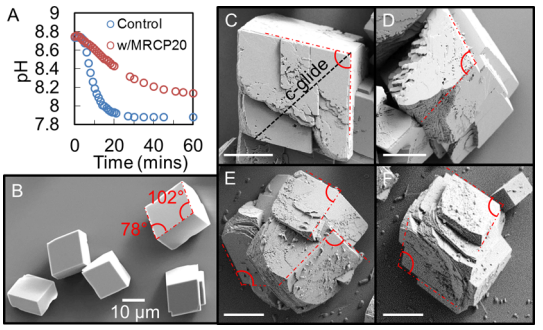

Figure 3. (A) pH drift showing inhibition of calcite formation by MRCP20 over time and (B–F) calcite microcrystals showing (B) no protein present and (C–F) crystals grown in the presence of MRCP20 showing selective inhibition of glide-symmetric crystal faces. Red lines indicate angles greater than 90° when viewed at an oblique angle, likely 102°. Scale bars represent 10 μm.

by thrombin protease. Purified MRCP20 with 6xHis exhibited 95% purity as assessed by gel electrophoresis (Figure 1A). The yield of recombinant MRCP20 isolated from expression in the periplasmic environment is approximately 1.5 mg/L of cell culture. The recombinant protein is largely soluble but also exists as polydispersed oligomeric species based on multiple peaks observed in the corresponding size-exclusion chromatograms. This distribution became monodispersed upon addition of 2-mercaptoethanol during purification, favoring a single lower molecular weight species seen by SDS-PAGE (Figure 1B). Circular dichroism (CD) measurements of the reduced form (Figure 1C) show a diminished curvature similar to previous work involving recombinant MRCP20 after exposure to 100 mM dithiothreitol.[18] Here, CD spectroscopy after purification and processing to remove reducing agents (Figure 1D) shows recovery of the MRCP20 secondary structure to previously established wild-type and recombinant forms.[18] Experiments in Figures 2, 3, and 5 were carried out using cleaved MRCP20 proteins, while Figure 4A was performed with His tag present. *Ex situ* AFM experiments in Figure 2B were performed with cleaved protein, verifying step-binding both with and without the tag.

Step Selectivity and Templating of Nanofibrils. As seen in Figure 2A, we directly observe how MRCP20 interacts with a $\{10\bar{1}4\}$ face of calcite and subsequent formation of nanofibrils on one set of unique steps through *in situ* ICM-AFM experiments under stagnant conditions. Concentrated MRCP20 solution was directly injected into the reservoir and observed over time to decorate steps adjacent to the in-plane 102° angle, related by a c-glide plane and represented in Figure 2A (ii, iii) by white dotted lines. This unique decoration was observed at multiple scanning locations and was not observed in the absence of the protein (Figure 2A (i)) while imaging bare calcite in DI H_2O prior to protein injection.

To observe the formation process of nanofibrils, separate *ex situ* experiments were carried out to image the templating process, as shown in Figure 2B. Here, individually cleaved calcite was incubated for 5, 300, and finally 7200 s in protein solution and rinsed in DI water prior to imaging in air. At 5 s, discrete monomers are seen to decorate the edges (<5 nm in size), forming short segments of linear fibrils by 300 s. Finally, at 7200 s calcite steps are observed to be completely saturated with fibrillar protein structures similar to those seen by *in situ* imaging. Cross-sectional analysis (Figure 2C) showed proteins to be roughly 1.5 nm in height, matching both the height of adsorbates from Figure 2A as well as the likely dimension of a smaller 20 kDa protein when compared to a larger 75 kDa streptavidin that is 4.6 nm wide.[22]

pH Drift and Vapor Mineralization. To measure the effect of MRCP20 on calcite mineralization, we continuously monitored pH under supersaturation conditions. As carbonate from $NaHCO_3$ is incorporated into growing calcite, protons are liberated and pH decreases

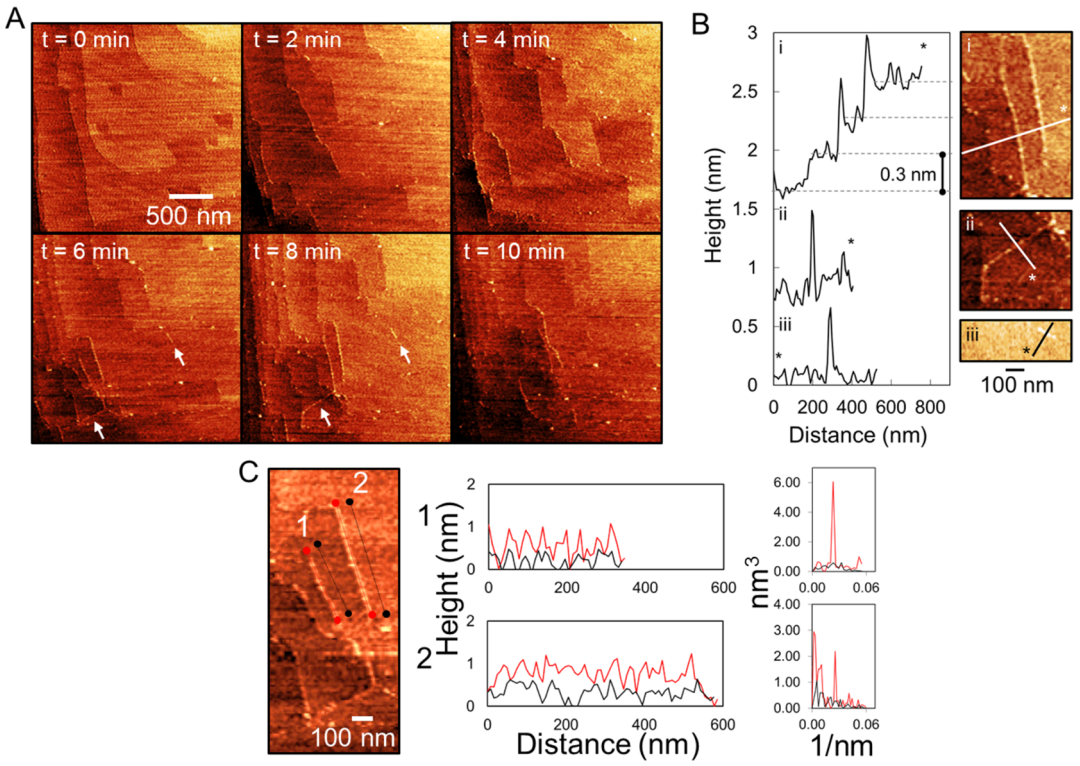

Figure 4. Structure and calcite interactions of protein fibrils by ICM-AFM. (A) *In situ* time-lapsed ICM-AFM of protein−calcite interaction over 10 min showing edge decoration, fibril formation, and enhanced dissolution of calcite. White arrows indicate observed off-edge fibrils. (B) Cross-sectional analysis of (i) fibrils on step edges and (ii, iii) isolated fibrils on terraces. (C) Striations are measured by cross-sectional height along the fibril axis to which power spectra are generated (right).

monotonically. Three distinct kinetic regimes are known to exist in calcite growth curves: a nucleation or incubation period, exponential growth, and last equilibrium.[23] Shown in Figure 3A, in the absence of protein, we observe the incubation period to last about 5 min before a drop in pH from growth, revealing a maximum rate of 0.12 pH units/min. In the presence of MRCP20, the incubation time is shortened to roughly 2 min but growth is slowed to a maximum rate of 0.02 pH/min or by roughly 85%. Shortening of the nucleation regime is likely due to the association of free ions such as calcium and carbonate to proteins. Both experiments reach equilibrium within 1 h. To determine whether the observed decrease in growth is due to solution or surface phenomena, we performed mineralization assays by introducing ammonium carbonate vapor through $CaCl_2$ and saline (KCl and NaCl) solution containing submerged glass coverslips. Control experiments showed well-formed rhombohedral calcite crystals with distinctive obtuse 102° and acute 78° corners. Final concentration of 0.03 mg/mL dialyzed protein was used to investigate MRCP20 morphogenic effects. Scanning electron microscope (SEM) imaging of representative etched crystals is shown in Figure 3C−F. As seen in Figure 3, MRCP20 exhibits a pronounced selective effect on crystal growth toward one set of faces to leave them rounded and inhibited. As marked by red lines, the opposing set of faces remains straight and joins at an obtuse 102° angle revealing a c-glide axis. We have observed this asymmetry across many crystals from multiple experiments (see Figure S2, Supporting Information). This result shows that under supersaturation MRCP20 selectively interacts with one set of enantiomorphic faces and frustrates growth to form asymmetric calcite crystals.

Formation, Structure, and Calcite Interactions of Fibrils by *in Situ* ICM-AFM. Time-lapse *in situ* ICM-AFM was used to directly observe the formation, structure, and surface interactions of protein nanofibrils on calcite $\{10\bar{1}4\}$ faces. Initially, calcite surfaces and step edges remain bare for 2 min before the protein solution reaches the surface at about 4 min (Figure 4A). Seen in the next few frames, steps oriented vertically in the image become preferentially occupied by fibrils, while horizontal steps remain bare. Over the course of the experiment, fibrils remain associated with steps and move in unison at a higher rate to create defects in the formerly straight bare step. In addition to step-associated fibrils, isolated off-edge fibrils were observed to exist as continuous linear segments spanning a few hundred nanometers; the fibrils were associated with calcite terraces with no alignment to existing step angles. As seen in Figure 4B, cross-sectional analysis of these fibrils further verifies that isolated fibrils (Figure 4B (ii, iii)) are not associated with an expected ca. 0.3 nm calcite step height seen with typical step-associated fibrils (Figure 4B (i)). The

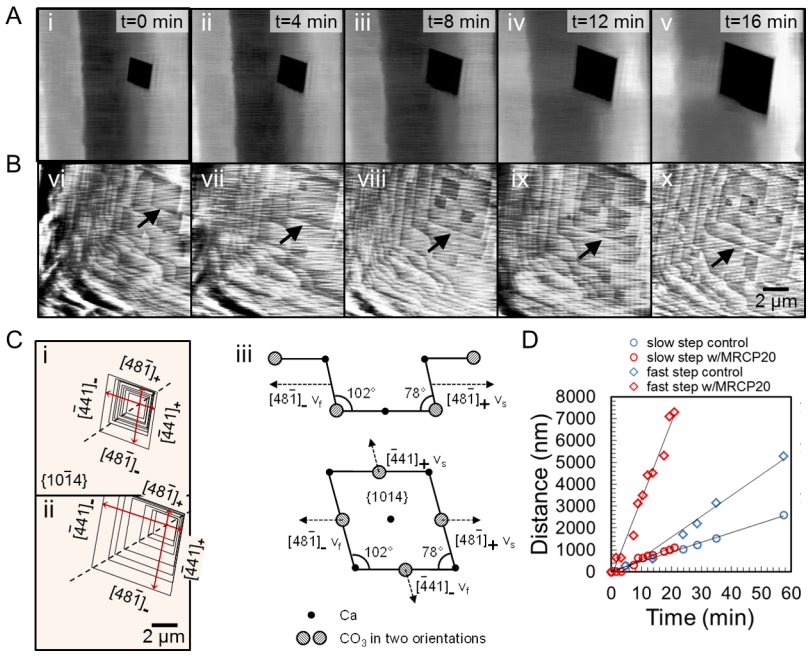

Figure 5. *In situ* **CM−AFM of calcite dissolution and in the presence of folded MRCP20. (A, i−v) Representative images of deep etch pit growth over 16 min at 4 min intervals. (B, vi−x) Base of etch pit after MRCP20 is introduced into the flow cell. Black arrows indicate the set of steps used to measure velocities in the presence of MRP20. (C, i−iii) AFM image overlays of etch pit movement over time with step orientations defined on the {10$\bar{1}$4} surface for (i) control and (ii) MRCP20. Dotted black line represents *c*-axis glide plane; red arrows indicate movement direction. (C, iii) (Top) in-plane and (bottom) out-of-plane bond angles for the {10$\bar{1}$4} surface atoms of calcite. (D) Plot of step movement over time for fast and slow steps both with (red) and without (blue) protein.**

existence of off-edge fibrils confirms that the observed protein structures are organized as continuous linear chains. Furthermore, striations were observed lengthwise along the fibrils in Figure 4. Using power spectrum analysis of the cross-sectional height along the fibrils, striations were measured to have a periodicity of 45 nm ±5 nm (see Figure 4C and Figure S3, Supporting Information). Step-mediated fibril formation was further observed in a separate experiment (see Figure S4, Supporting Information) where straight step edges became rounded and decorated with particles (*ca.* 5−10 nm in size) that appear to be monomeric or clustered protein. Over time, discrete particles became linear fibrils and continued to occupy the step edge as they moved under dissolution. Optical micrographs of the protein-reacted surfaces after AFM experiments reveal numerous etch pits larger than 100 μm (see Figure S5, Supporting Information), much larger than etch pits formed in water alone.

Bulk Protein Interactions with Calcite Etch Pits by *in Situ* CM-AFM. To directly observe calcite surface features and their modification upon protein interaction, we tracked the lateral growth rate of deep and shallow rhombohedral etch pits on freshly cleaved {10$\bar{1}$4} calcite surfaces by *in situ* CM-AFM (Figure 5A,B). Upon close inspection of Figure 5, steps appear bare with no step-associated proteins or fibrils seen previously by ICM-AFM, yet large shifts in step velocities are observed when protein is introduced. CM-AFM experiments, therefore, are used here as an indication of calcite step interactions with bulk protein solutions as assumed in prior studies.[24,25] Contact mode imaging affords stability and low lateral scanner drift over tens of microns to quantify etch pit evolution.[26,27] Under dissolution, the velocity of etched geometries defined by steps reveals the crystal orientation of surface features.[28−30] Here, rhombohedra on the {10$\bar{1}$4} face are defined by two sets of [48$\bar{1}$] and [$\bar{4}$41] steps joined by acute 78° and obtuse 102° in-plane angles. One set lies obtuse to the {10$\bar{1}$4} plane while the other lies acute, and each set is related through glide-plane symmetry. Overlaid etch pit outlines in Figure 5C (i, ii) show two sets of step edges dissolving at different rates, leading to anisotropic enlargement of overall rhombohedra. As also shown in Figure 5C (iii), acute and obtuse angles define two kink geometries at equivalent step sites leading to

TABLE 1. Step Velocities As Measured from Figure 3 and Correlation to Line Fitted by Sum of Least-Squares Regression

	control	MRCP20
v_f (nm s^{-1})	1.6	5.9
SE_m[a] (nm s^{-1})	±0.1	±0.3
v_s (nm s^{-1})	0.7	0.9
SE_m (nm s^{-1})	±0.02	±0.06
v_f/v_s	2.1 ± 0.2	6.2 ± 0.7

[a] SE_m refers to the standard error of the slope of linear regression.

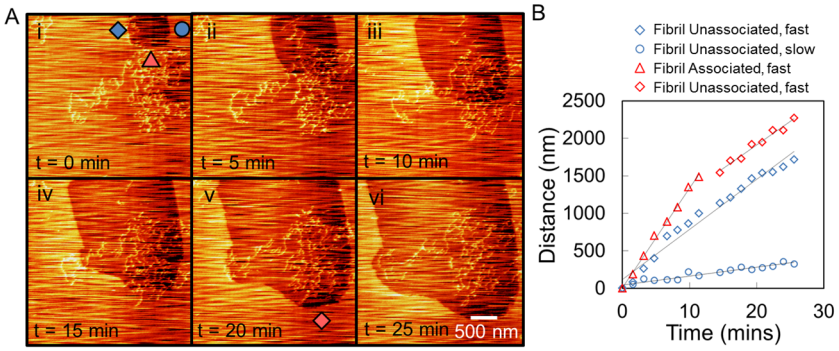

Figure 6. (A, i–vi) Representative *in situ* AFM images of a single-layer etch pit growing under constant association with MRCP20 fibrils. (B) Plot of quantified fast and slow step movements over time. Red markings indicate a step that is fibril-associated for 10 min during i–iii but unassociated from iv to vi.

both fast- (v_f) and slow-moving (v_s) [48$\bar{1}$] and [$\bar{4}$41] steps. The first frame of Figure 5A shows an isolated, pre-existing pit ca. 30 nm deep with a half-maximum width of *ca.* 1.2 μm. Over the course of 1 h, this pit grows to a size of ca. 10 μm × 10 μm in dimension. As summarized in Table 1, we measure v_f = 1.6 ± 0.1 nm s^{-1} and v_s = 0.7 ± 0.02 nm s^{-1} for calcite dissolving in solution, which yields a v_f/v_s ratio of 2.1 ± 0.2. These values are in agreement with Liang *et al.*'s ratio of 2.3, where v_f = 3.4 nm s^{-1} and v_s = 1.5 nm s^{-1}.[30] In addition to equivalent step lengths as measured by AFM from observed rhombohedra, a linear relation between edge length and time further verifies that step migration in etch pits originates from a single dislocation with no interstep interactions.

After 1.5 h of dissolution, MRCP20 is introduced into the flow cell, and protein interaction with calcite is observed by time-lapse microscopy as represented in Figure 5B (vi–x). During 30 min of exposure to protein, the etch pit exceeds the scan size as the pit wall moves outside of the scanning window, leaving just the base of the pit from Figure 5B (vii–x). Isolated surface rhombohedra grow with significantly different rates upon exposure to MRCP20 and can be compared to deep etch pit growth rates. Ramensee *et al.* demonstrated comparable step velocities between deep etch pits and shallow surface rhombohedra as no interstep interactions occur in either case.[28] As seen in Figure 5D, by measuring step displacement over time, slow steps have a velocity v_s= 0.9 ± 0.06 nm s^{-1} while fast steps move at v_f = 5.9 ± 0.3 nm s^{-1} to yield a v_f/v_s = 6.2 ± 0.7. While the enhancement of the slow step dissolution was only ~30%, obtuse steps moved about 4-fold faster than calcite in H_2O and clearly demonstrate a greater than 10-fold selectivity for fast-moving calcite steps by MRCP20. Large-scale optical micrographs collected on a calcite specimen after AFM experiments show both significant enlargement of etch pits compared to the control as well as enlargement across multiple pit features (see Figure S5, Supporting Information). Enhancement in one set of glide-symmetric steps seen in CM-AFM is consistent with calcite microcrystals grown in the presence of MRCP20 (Figure 3), where asymmetric crystals are also defined by a set of rounded enantiomorphic faces.

TABLE 2. List of Fast and Slow Step Velocities Measured from Fibril-Associated and -Unassociated Step Movement over Time and Their Ratios

	fibril associated	fibril unassociated
v_f (nm s^{-1})	2.2	1.1
SE_m[a] (nm s^{-1})	±0.06	±0.05
v_s (nm s^{-1})	0.2	0.2
SE_m (nm s^{-1})	±0.01	±0.01
v_f/v_s	11.0 ± 0.8	5.6 ± 0.5

[a] SE_m refers to the standard error of the slope of linear regression.

Nanofibril Interactions with Calcite Etch Pits by *in Situ* CM-AFM. Due to greater shear forces exhibited by CM-AFM than ICM-AFM, step-associated nanofibrils were not observable in deep etch pit experiments; however, after 1 h of constant scanning by CM-AFM, displaced fibrils (Figure 6) began to appear on calcite terraces. To stably image the fibrils, we reduced the effective scan rate to one-third of prior imaging conditions by lowering the scan size to 5 μm^2. The existence of surface-associated nanofibrils provides an opportunity to directly observe how step velocities are impacted by MRCP20 in fibril form. Shown in Figure 6, a single-layer etch pit grows directly under surface-associated fibrils to reveal localized etching that reflects selectivity for fast moving steps similar to observations in Figure 5. As detailed in Table 2, nonfibril-associated fast and slow steps are measured to be v_f = 1.1 ± 0.05 nm s^{-1} and v_s = 0.2 ± 0.01 nm s^{-1} with a v_f/v_s ratio of 5.6 ± 0.5, similar to the previously measured ratio in the presence of MRCP20. Interestingly, steps moving beneath protein fibrils accelerate to v_f = 2.2 ± 0.06 nm s^{-1} or nearly twice the rate of unassociated steps with a v_f/v_s of 11.0 ± 0.8. Once the step clears the associated protein fibrils, its velocity returns to the speed of unassociated steps, or 1.05 ± 0.05 nm s^{-1}. Over the same time period, the remaining slow-moving step maintains a straight edge whether associated

or unassociated with protein fibrils, indicating that proteins have little effect on slow moving acute steps.

DISCUSSION

The molecular basis for calcite step selection has been well-studied. Mori *et al.* implicated MRCP20 as calcite-specific due to its high levels of aspartic acid (11.5%) and glutamic acid (10.4%),[18] which have been previously established to interact specifically with acute calcite steps through bidentate interactions with calcium cations, afforded by side-chain carboxylic acids.[13,31] Using L- or D-homochiral Asp solutions, Orme *et al.* observed this interaction to break the crystal symmetry of formed mineral in favor of only one of two respective glide-symmetric acute steps dependent on the chirality of Asp.[13] Unlike single Asp residues, MRCP20 displays equal binding and enhanced dissolution on both enantiomorphic obtuse steps. Obtuse step selectivity has been reported for other prototypical acidic proteins such as ovalbumin (pI = 4.6) under supersaturated conditions,[25,32] which also stands in contrast to acute step selectivity found in single residues of Asp.[13] Larger acidic peptides and abalone shell proteins have also demonstrated apparent geometric selectivity in favoring interaction with obtuse steps over acute ones.[12,25,32,33] Work by Elhadj *et al.* showed that Asp_n peptides with $n = 1-6$ demonstrated a switch from acute to obtuse steps at n = 2, explained through semiquantum mechanical calculations as varying dehydration energies between steps.[12] Additional steric constraints brought about by secondary and tertiary protein structures inherent to MRCP20, including a surface-bound height of 1−2 nm measured by *in situ* AFM, could prevent acidic side chains from coordinating calcium atoms in recessed acute steps. Reduced free cysteine residues have been observed to interact with and incorporate into growing mineral phase as highly as Asp; however, these residues are disulfide bonded in folded MRCP20.[34]

We observed a large difference in rates of obtuse step movement under surface-associated fibrils compared to bulk solution proteins, highlighting the impact of stable surface-bound protein nanostructures in shaping calcite. Throughout all experimental data in which fibrils were observed in this work, associated steps are accelerated over bare steps when exposed to bulk protein solution. Both bulk protein and fibrils maintain similar selective interactions to accelerate the movement of mainly the obtuse calcite steps. Since fibrils are formed only on obtuse steps, the acceleration of step-edge dissolution measured in their presence is likely due to permanent surface association, while bulk proteins maintain reversible binding kinetics with steps. We measured this to be a 2-fold enhancement, as surface-bound structures enable proteins to remain localized at atomic features and maintain interactions with both the underlying step and immediate solution environment.

Although the internal structure of assembled protein fibrils remains a challenge to resolve, they likely maintain a degree of order as seen in other surface-templated biomolecular systems.[35] Upon close inspection of *in situ* data from Figure 4, fibrils maintain striations with a period of 45 nm ±5 nm (see Figure 4C and Figure S3, Supporting Information) as measured in the power spectrum of lengthwise cross-sectional height data. As we observed adsorption, aggregation, and fibril formation directly on steps, as well as evidence that these structures are continuous when displaced from steps, it is likely that they exhibit some degree of registry with step-edge atoms. Such lattice-matching mechanisms require repetitive sequence motifs in the protein which would allow for alignment with calcite. MRCP20 is composed of six homologous sequence domains (see Figure 1A), where each domain includes a proline−cysteine pair in the same residue position when aligned by domain. As prolines commonly dictate the direction of the polypeptide chain, such as in β turns, this motif could be responsible for aligning and assembling observed protein nanofibrils with calcite steps. The largely disordered random coil conformation of MRCP20 in bulk solution indicates that this protein likely undergoes disorder-to-order transition upon encountering periodic surface features similar to other disordered protein and peptide interactions with solids.[10,36] Previous *in vitro* efforts to form fibrils in solution from individual barnacle proteins have been successful by generating unstable peptide segments of parent proteins.[19,37] In contrast, our work here shows that interactions with periodic surface features can serve to destabilize intact cement proteins in forming nanostructured fibrils.

Recent transcriptome analysis of the membranous barnacle *Tetraclita japonica formosana* by Lin *et al.* has revealed an absence of a MRCP20-homologue.[38] This homologue has been found in all sequencing studies done on barnacles that maintain calcareous base plates, consistent with the possibility that this protein is active at the base plate−cement interface as implicated in a recent review of the subject.[39] As barnacles require methods of forming and reshaping the overall base plate, as well as various asymmetric channel substructures within, proteins such as MRCP20 could determine the direction of crystal chains or orientations of crystals themselves.

CONCLUSION

In this work, we report the *in vitro* observation of molecular self-assembly by an isolated and intact barnacle cement protein at a marine relevant liquid−solid interface. The arrangement of raised atomic surface features plays a key role in the binding specificity

of MRCP20 with calcite, where proteins bind only to step geometries that lie obtuse to the $\{10\bar{1}4\}$ surface plane. In the process of interacting with obtuse steps, MRCP20 proteins are templated into striated long-range protein nanofibrils that in turn preferentially dissolve step edges of the same atomic arrangement. Through multiple calcite experiments, we show that step preference by MRCP20 is not enantiomorphic as both mirror-symmetric obtuse steps are modified. Templated surface nanofibrils exhibit up to a 2-fold enhancement of dissolving obtuse steps, implying that cooperativity plays a large role in enhancing the activity of MRCP20. As nanofibrils are also a significant component in secreted barnacle cement, our work demonstrates potential new molecular strategies evolved by barnacles to adhere and manipulate calcite through cooperative surface-templated biomolecular structures.

METHODS

Materials. Analytical-grade calcium chloride dihydrate, sodium bicarbonate, phosphate-buffered saline (working concentration of 0.01 M phosphate, 0.138 M NaCl, 2.7 mM KCl, pH 7.4), Tris HCl, ammonium carbonate, sodium chloride, potassium chloride, sodium hydroxide, and hydrogen chloride were purchased from Sigma-Aldrich (St. Louis, MO). All water used was deionized and filtered through a Millipore (Billerica, MA) Milli-Q system with resistivity of >18 mΩ. All restriction enzymes and T4 DNA ligase used in this study were purchased from New England Biolabs (Ipswich, MA).

Preparation of Recombinant MRCP20. The MRCP20 gene sequence was obtained using accession no. AB035415 through Genbank. DNA sequence encoding MRCP20 was synthesized and cloned into shuttle plasmids for amplification by Eurofins Genomics (Huntsville, AL). Synthesized MRCP20 gene was inserted into pet22b via MscI and XhoI to yield the plasmid pet22b-MRCP20. A thrombin cleavage sequence, LVPRGS, was then inserted between MRCP20 and a C-terminal His-tag by PCR cloning into pet22b using MscI and XhoI sites. MRCP20-LVPRGS-pet22b plasmids were then transformed to a host expression strain, Tuner (DE3) (EMD Millipore, Billerica, MA), for protein expression. Transformed cells were subsequently plated onto Lysogeny broth (LB) agar plates and inoculated overnight in 250 mL of Terrific Broth (TB) media containing ampicillin. For expression, cultures were scaled up to 500 mL of TB and incubated for 4 h before the addition of 0.5 mM isopropyl β-D-1-thiogalactopyranoside (IPTG) at an optical density of roughly 0.8 at 600 nm. Cells were induced first at 30 °C for 2 h and then overnight at 20 °C and were pelleted at 5000*g* for 10 min. To isolate MRCP20 protein, the osmotic shockate was prepared according to Nossel and Heppel[40] and subjected to metal affinity chromatography (Ni-NTA, Qiagen, Valencia, CA) followed by size-exclusion chromatography (Superdex 75, GE Healthcare, Pittsburgh, PA) in the presence of reducing agent 2-mercaptoethanol using the AKTA system (Amersham Bioscience, Amersham, UK).[41,42] The eluted protein was loaded onto 10% NuPAGE Bis-Tris gel and separated using 2-(*N*-morpholino)ethanesulfonic acid SDS (MES-SDS) running buffer (Life Technologies, Grand Island, NY).

To remove the C-terminal His-tag, purified MRCP20-LVPRGS-His was incubated in biotinylated thrombin solution (EMD Millipore, Billerica, MA) for 24 h and separated first by a streptavidin−agarose column (EMD Millipore, Billerica, MA) and subsequently with Ni-NTA-functionalized agarose (Qiagen, Valencia, CA) following the manufacturer's protocol. Prior to use, protein solutions were passed through a 5 mL Hi-Trap solvent exchange column packed with Sephadex G25 Super-Fine resin (GE Healthcare, Pittsburgh, PA). This step was found to effectively remove excess or bound reducing agent, 2-mercaptoethanol. Cleaved proteins were separated by electrophoresis and isolated for sequence analysis by mass spectrometry to confirm the cleavage of 6xHis.

Circular Dichroism. A JASCO (Easton, MD) J-815 CD spectrometer was used to collect CD spectra over the wavelength range of 195−250 nm at a scan rate of 20 nm min^{-1} averaging over three accumulations. All obtained spectra were baseline corrected using 0.01 M phosphate-buffered saline and converted from raw ellipticity (θ) to mean residue molar ellipticity ($[\theta]$) by the following equation

$$[\theta] = \frac{\theta \times MW_i}{10000 \times C_i \times L \times N_i}$$

where MW_i is the molecular weight of the protein (g mol^{-1}), C_i is the protein concentration (g mL^{-1}), L is the optical path length through solvent (cm), and N_i is the number of residues.

pH Drift. MRCP20 solutions were dialyzed against 7.5 mM $CaCl_2$ as previously described. To initiate mineralization, reagents were added stepwise into a round-bottom flask placed in a circulating water bath maintained at 20.0 °C. The initial incubation medium included 28.1 mL artificial seawater (ASW: 0.5 M NaC1 and 0.011 M KC1) to which 0.3 mL of 1.0 M $CaCl_2$ was added to obtain 10 mM calcium. Next, 1 mL of protein solution (0.3 mg/mL) was added and the mixture stirred for 10 min. Finally, 0.6 mL of 0.4 M $NaHCO_3$ was added to yield 8 mM dissolved inorganic carbon, and the solution was titrated to a pH of 8.30 with 0.1 M NaOH to begin the assay. The final protein concentration was 0.01 mg/mL.

Fluid-Mode AFM under Flow. A Nanoman AFM (Veeco, Santa Barbara, CA) housed in an acoustic isolation chamber was equipped with a direct-drive tip holder made from polychlorotrifluoroethylene for fluid scanning (DECAFMCH-DD, Bruker, Camarillo, CA) operating in contact or intermittent contact mode (CM or ICM) with an external Nanoscope V controller (Bruker, Santa Barbara, CA) to collect topographic images and quantify calcite dissolution rates *in situ*. Triangular probes (Sharp Nitride Levers, 0.12 N/m, Bruker AFM Probes, Camarillo, CA) were used where thin and flexible silicon nitride cantilevers with sharp silicon tips (nom radii of 2 nm) for high resolution *in situ* imaging of protein molecules on calcite. For optimum surface tracking and imaging, cantilevers were first tuned in fluid at ca. 27 kHz followed by a manual approach using the step-motor function. The amplitude set point was established by monitoring the amplitude response in real-time continuous ramping mode while lowering the tip ca. 100 nm per step. A sharp linear decline in cantilever amplitude versus z-piezo distance establishes the intermittent contact regime between the tip and the surface. To minimize applied force, the amplitude at 90% of this intermittent regime was used as the set point for imaging in fluid.

Geological calcite (Icelandic Spar, Chihuahua, Mexico) was freshly cleaved prior to each experiment by gentle knocking with the blunt end of a screwdriver while wrapped in lint-free wipes. Crystals roughly 3 × 3 × 4 mm in size were immediately fixed to a standard glass microscope slide using low-temperature thermosetting epoxy (Shell, EPON Resin 1004F) and blown dry with nitrogen to remove debris from the cleavage. Glass slides were cleaned of organic contaminants by piranha rinse (3:1 H_2SO_4/H_2O_2; warning: highly volatile; follow appropriate safety precautions) prior to mounting. For AFM, glass slides were fitted with a custom cylindrical Teflon reservoir 2.5 mm high × 20 mm in diameter, which accommodates the tip-holder while compressing a 1-in. Viton O-ring to seal both glass and calcite during imaging. The reservoir volume was 1 mL. Flow was generated by a peristaltic pump (Masterflex, Cole-Parmer, Vernon Hills, IL) with tubing connected to an inlet of the reservoir at a rate

of 0.5 mL/min. Outflow from the reservoir was run into a beaker as waste. Liquid flow parallel to the mounted calcite surface plane was obtained by placing the inlet and outlet laterally adjacent to the sample. Premixed protein solution (0.01 mg/mL, pH 8.5) and DI water were stored separately in 60 mL vessels upstream of the pump and were separated by a three-way selector valve, all contained within the acoustic chamber. Protein solutions, tubing, and flow cell were equilibrated overnight inside the acoustic chamber prior to experiments. Control experiments were run for *ca.* 30 min prior to data collection to thermally equilibrate both the tip and mounted calcite sample.

Images varying in dimension were typically scanned at 3 Hz at a resolution of 384 × 512 data points. *Ex situ* imaging was performed on calcite after the sample had been serially dilution rinsed with DI water and dried under nitrogen gas.

Large-scale scanning probe experiments were carried out in deflection mode using the same flow cell and experimental protocol as in ICM-AFM experiments. One hour prior to experiments, mounted scanning probes were placed in the fluid tip holder and equilibrated in the flow cell with DI water and freshly cleaved calcite. All materials exposed to calcite surfaces were incubated in the closed acoustic chamber overnight. A deflection set point of 0.1 V was used to minimize shear forces applied to the surface during imaging, with a scan rate of 4 Hz. The system was run for 30 min prior to data collection to reach thermal equilibrium. To minimize effects from variability in natural calcite impurities,[43] all experimental data were collected from one bulk calcite crystal and all CM-AFM data were collected (Figures 5 and 6) from the same rhombohedral etch pit.

All AFM image processing, step-edge measurements, cross sections, and power spectral analyses were carried out using ImageJ 1.49f (NIH, USA), WxSM 5.0d7 (Nanotec Electronica, Spain) and Gwyddion 2.37 (Czech Metrology Institute, Czech Republic) software.

Step-Edge Measurement. Step-edge velocity was measured as displacement over time by subtracting the initial step distance from each subsequent step, measured as the distance between the edge and a bisecting line through the first observed rhombus. For the growth rate of deep etch pits, edge movement was measured from the center of the pit to the half-maximum pit wall height (see Figure S1, Supporting Information). Rates were determined by the slope of a least-squares linear regression analysis on temporal displacement data, and the associated error is the standard error of the regression slope (SE_m)

$$\mathrm{SE}_m = \sqrt{\sum((y_i - \hat{y}_i)^2)/(n-2)} / \sqrt{\sum((x_i - \bar{x}))^2}$$

where y_i is the observed distance $\hat{y}_i$ is the estimated distance by linear regression, x_i is the observed time in min, $\bar{x}$ is the mean of the image capture times, and n is the population size.

Mineralization by Vapor Diffusion. Slow-growth mineralization experiments were performed on submerged glass coverslips following the well-established technique of ammonium carbonate vapor diffusion through a calcium chloride solution.[17,25] Coverslips were cleaned for 30 min in 70% H_2SO_4 and 30% H_2O_2 using a grooved trough-style ceramic vessel to keep surfaces separated during cleaning. Coverslips were rinsed in deionized water (18.1 mΩ) and placed in a Nunc six-well plate (Nalgene, Rochester, NY), each submerged in 7.5 mM $CaCl_2$ solution. MRCP20 stored in phosphate-buffered saline was dialyzed twice (Spectra/Por 7 MWCO: 10000, Spectrum Laboratories, Rancho Dominguez, CA) against 7.5 mM $CaCl_2$ for 3 h at room temperature and adjusted to pH 7.5 by a dropwise addition of 0.1 M NaOH. Final protein solutions were 0.02 mg/mL. Well plates were wrapped in aluminum foil, punctured with two pin holes, and placed in a small desiccator also containing a beaker of ammonium carbonate. Samples were left for 7 days before removal and SEM characterization.

Scanning Electron Microscopy. Calcite crystals were characterized by SEM using a Supra 55 field emitting microscope (Carl Zeiss Microscopy, DE) operating at a beam voltage of 2.0 kV and working distance of *ca.* 4 mm. After completion of the crystallization experiments, glass coverslips containing calcite particles were affixed to aluminum SEM mounts using carbon tape. To ensure a conductive pathway through the sample mount, carbon tape was wrapped around coverslips so that a small portion of the tape was in contact with the glass surface and further sputter coated with 3.0 nm of gold.

Conflict of Interest: The authors declare no competing financial interest.

Acknowledgment. This work was supported by the Basic Research Program of the Naval Research Laboratory (NRL) and through the Office of Naval Research Coatings Program. C.R.S. was supported through a National Research Council Postdoctoral Research Associateship. We gratefully acknowledge J. Scancella for assistance with mineralization assays. We also thank J. Weimer, D. Barlow, and C. Spillmann for helpful discussions.

Supporting Information Available: Additional microscopy images, fibril measurements, deep etch-pit AFM cross sections, and time-lapse AFM movies. The Supporting Information is available free of charge on the ACS Publications website at DOI: 10.1021/acsnano.5b01870.

REFERENCES AND NOTES

1. Fratzl, P.; Gupta, H. S.; Paschalis, E. P.; Roschger, P. Structure and Mechanical Quality of the Collagen-Mineral Nano-Composite in Bone. *J. Mater. Chem.* **2004**, *14*, 2115–2123.
2. Wassen, M. H.; Lammens, J.; Tekoppele, J. M.; Sakkers, R. J.; Liu, Z.; Verbout, A. J.; Bank, R. A. Collagen Structure Regulates Fibril Mineralization in Osteogenesis as Revealed by Cross-Link Patterns in Calcifying Callus. *J. Bone Miner. Res.* **2000**, *15*, 1776–1785.
3. Moradian-Oldak, J. Amelogenins: Assembly, Processing and Control of Crystal Morphology. *Matrix Biol.* **2001**, *20*, 293–305.
4. Veis, A. Mineral-Matrix Interactions in Bone and Dentin. *J. Bone Miner. Res.* **1993**, *8*, S493–S497.
5. Jin, T.; Ito, Y.; Luan, X.; Dangaria, S.; Walker, C.; Allen, M.; Kulkarni, A.; Gibson, C.; Braatz, R.; Liao, X.; et al. Elongated Polyproline Motifs Facilitate Enamel Evolution through Matrix Subunit Compaction. *PLoS Biol.* **2009**, *7*, e1000262.
6. Brown, C. L.; Aksay, I. A.; Saville, D. A.; Hecht, M. H. Template-Directed Assembly of a de Novo Designed Protein. *J. Am. Chem. Soc.* **2002**, *124*, 6846–6848.
7. Kang, S.; Li, H.; Huynh, T.; Zhang, F.; Xia, Z.; Zhang, Y.; Zhou, R. Molecular Mechanism of Surface-Assisted Epitaxial Self-Assembly of Amyloid-like Peptides. *ACS Nano* **2012**, *6*, 9276–9282.
8. Zhang, F.; Du, H.-N.; Zhang, Z.-X.; Ji, L.-N.; Li, H.-T.; Tang, L.; Wang, H.-B.; Fan, C.-H.; Xu, H.-J.; Zhang, Y.; et al. Epitaxial Growth of Peptide Nanofilaments on Inorganic Surfaces: Effects of Interfacial Hydrophobicity/hydrophilicity. *Angew. Chem., Int. Ed.* **2006**, *45*, 3611–3613.
9. So, C. R.; Hayamizu, Y.; Yazici, H.; Gresswell, C.; Khatayevich, D.; Tamerler, C.; Sarikaya, M. Controlling Self-Assembly of Engineered Peptides on Graphite by Rational Mutation. *ACS Nano* **2012**, *6*, 1648–1656.
10. So, C. R.; Kulp, J. L.; Oren, E. E.; Zareie, H.; Tamerler, C.; Evans, J. S.; Sarikaya, M. Molecular Recognition and Supramolecular Self-Assembly of a Genetically Engineered Gold Binding Peptide on Au{111}. *ACS Nano* **2009**, *3*, 1525–1531.
11. Wolf, S. E.; Loges, N.; Mathiasch, B.; Panthöfer, M.; Mey, I.; Janshoff, A.; Tremel, W. Phase Selection of Calcium Carbonate through the Chirality of Adsorbed Amino Acids. *Angew. Chem., Int. Ed.* **2007**, *46*, 5618–5623.
12. Elhadj, S.; Salter, E. A.; Wierzbicki, A.; Yoreo, J. J. De; Han, N.; Dove, P. M. Peptide Controls on Calcite Mineralization: Polyaspartate Chain Length Affects Growth Kinetics and Acts as a Stereochemical Switch on Morphology. *Cryst. Growth Des.* **2006**, *6*, 197–201.
13. Orme, C. A.; Noy, A.; Wierzbicki, A.; McBride, M. T.; Grantham, M.; Teng, H. H.; Dove, P. M.; DeYoreo, J. J. Formation of Chiral Morphologies through Selective Binding of Amino Acids to Calcite Surface Steps. *Nature* **2001**, *411*, 775–779.

14. Barlow, D. E.; Dickinson, G. H.; Orihuela, B.; Rittschof, D.; Wahl, K. J. *in Situ* ATR-FTIR Characterization of Primary Cement Interfaces of the Barnacle *Balanus amphitrite*. *Biofouling* **2009**, *25*, 359–366.
15. Barlow, D. E.; Dickinson, G. H.; Orihuela, B.; Kulp, J. L.; Rittschof, D.; Wahl, K. J. Characterization of the Adhesive Plaque of the Barnacle *Balanus amphitrite*: Amyloid-like Nanofibrils Are a Major Component. *Langmuir* **2010**, *26*, 6549–6556.
16. Addadi, L.; Weiner, S. Interactions between Acidic Proteins and Crystals: Stereochemical Requirements in Biomineralization. *Proc. Natl. Acad. Sci. U.S.A.* **1985**, *82*, 4110–4114.
17. Mann, K.; Siedler, F.; Treccani, L.; Heinemann, F.; Fritz, M. Perlinhibin, a Cysteine-, Histidine-, and Arginine-Rich Miniprotein from Abalone (*Haliotis laevigata*) Nacre, Inhibits *in Vitro* Calcium Carbonate Crystallization. *Biophys. J.* **2007**, *93*, 1246–1254.
18. Mori, Y.; Urushida, Y.; Nakano, M.; Uchiyama, S.; Kamino, K. Calcite-Specific Coupling Protein in Barnacle Underwater Cement. *FEBS J.* **2007**, *274*, 6436–6446.
19. Nakano, M.; Shen, J.-R.; Kamino, K. Self-Assembling Peptide Inspired by a Barnacle Underwater Adhesive Protein. *Biomacromolecules* **2007**, *8*, 1830–1835.
20. Kamino, K. Novel Barnacle Underwater Adhesive Protein Is a Charged Amino Acid-Rich Protein Constituted by a Cys-Rich Repetitive Sequence. *Biochem. J.* **2001**, *356*, 503–507.
21. He, L.-S.; Zhang, G.; Qian, P.-Y. Characterization of Two 20 kDa-Cement Protein (cp20k) Homologues in *Amphibalanus Amphitrite*. *PLoS One* **2013**, *8*, e64130.
22. Hendrickson, W. A.; Pähler, A.; Smith, J. L.; Satow, Y.; Merritt, E. A.; Phizackerley, R. P. Crystal Structure of Core Streptavidin Determined from Multiwavelength Anomalous Diffraction of Synchrotron Radiation. *Proc. Natl. Acad. Sci. U.S.A.* **1989**, *86*, 2190–2194.
23. Gunthorpe, M.; Sikes, C.; Wheeler, A. Promotion and Inhibition of Calcium Carbonate Crystallization *in Vitro* by Matrix Protein from Blue Crab Exoskeleton. *Biol. Bull. (Woods Hole, MA, U.S.)* **1990**, *179*, 191–200.
24. Kim, I. W.; Darragh, M. R.; Orme, C.; Evans, J. S. Molecular "Tuning" of Crystal Growth by Nacre-Associated Polypeptides. *Cryst. Growth Des.* **2006**, *6*, 5–10.
25. Zhao, K.; Wang, M.; Wang, X.; Wu, C.; Xu, H.; Lu, J. R. Crystal Growth of Calcite Mediated by Ovalbumin and Lysozyme: Atomic Force Microscopy Study. *Cryst. Growth Des.* **2013**, *13*, 1583–1589.
26. Qiu, S. R.; Orme, C. A. Dynamics of Biomineral Formation at the near-Molecular Level. *Chem. Rev.* **2008**, *108*, 4784–4822.
27. Morse, J. W.; Arvidson, R. S.; Lüttge, A. Calcium Carbonate Formation and Dissolution. *Chem. Rev.* **2007**, *107*, 342–381.
28. Jordan, G.; Rammensee, W. Dissolution Rates of Calcite (1014) Obtained by Scanning Force Microscopy: Microtopography-Based Dissolution Kinetics on Surfaces with Anisotropic Step Velocities. *Geochim. Cosmochim. Acta* **1998**, *62*, 941–947.
29. Liang, Y.; Baer, D. Interplay between Step Velocity and Morphology during the Dissolution of CaCO3 Surface. *J. Vac. Sci. Technol., A* **1996**, *14*, 1368–1375.
30. Liang, Y.; Baer, D.; McCoy, J. Dissolution Kinetics at the Calcite-Water Interface. *Geochim. Cosmochim. Acta* **1996**, *60*, 4883–4887.
31. Teng, H.; Dove, P. Surface Site-Specific Interactions of Aspartate with Calcite during Dissolution: Implications for Biomineralization. *Am. Mineral.* **1997**, *82*, 878–887.
32. Wang, X.; Wu, C.; Tao, K.; Zhao, K.; Wang, J.; Xu, H.; Xia, D.; Shan, H.; Lu, J. R. Influence of Ovalbumin on CaCO3 Precipitation during *in Vitro* Biomineralization. *J. Phys. Chem. B* **2010**, *114*, 5301–5308.
33. Elhadj, S.; De Yoreo, J. J.; Hoyer, J. R.; Dove, P. M. Role of Molecular Charge and Hydrophilicity in Regulating the Kinetics of Crystal Growth. *Proc. Natl. Acad. Sci. U.S.A.* **2006**, *103*, 19237–19242.
34. Borukhin, S.; Bloch, L.; Radlauer, T.; Hill, A. H.; Fitch, A. N.; Pokroy, B. Screening the Incorporation of Amino Acids into an Inorganic Crystalline Host: The Case of Calcite. *Adv. Funct. Mater.* **2012**, *22*, 4216–4224.
35. Kang, S.; Huynh, T.; Xia, Z.; Zhang, Y.; Fang, H.; Wei, G.; Zhou, R. Hydrophobic Interaction Drives Surface-Assisted Epitaxial Assembly of Amyloid-like Peptides. *J. Am. Chem. Soc.* **2013**, *135*, 3150–3157.
36. Goobes, G.; Goobes, R.; Schueler-Furman, O.; Baker, D.; Stayton, P. S.; Drobny, G. P. C-terminal Bacterial Binding Domain in Statherin upon Adsorption onto Hydroxyapatite Crystals. *Proc. Natl. Acad. Sci. U. S. A.* **2006**, *103*, 16083–16088.
37. Nakano, M.; Kamino, K. Amyloid-like Conformation and Interaction for the Self-Assembly in Barnacle Underwater Cement. *Biochem.* **2015**, *54*, 826–835.
38. Lin, H.; Wong, Y.; Tsang, L.; Chu, K.; Qian, P.; Chan, B. First Study on Gene Expression of Cement Proteins and Potential Adhesion-Related Genes of a Membranous-Based Barnacle as Revealed from Next-Generation Sequencing Technology. *Biofouling* **2014**, *30*, 169–181.
39. Kamino, K. Mini-Review: Barnacle Adhesives and Adhesion. *Biofouling* **2013**, *29*, 735–749.
40. Nossel, N.; Heppel, L. The Release of Enzymes by Osmotic Shock from *Escherichia coli* in Exponential Phase. *J. Biol. Chem.* **1966**, *241*, 3055–3062.
41. Liu, J. L.; Anderson, G. P.; Delehanty, J. B.; Baumann, R.; Hayhurst, A.; Goldman, E. R. Selection of Cholera Toxin Specific IgNAR Single-Domain Antibodies from a Naive Shark Library. *Mol. Immunol.* **2007**, *44*, 1775–1783.
42. Hayhurst, A.; Happe, S.; Mabry, R.; Koch, Z.; Iverson, B. L.; Georgiou, G. Isolation and Expression of Recombinant Antibody Fragments to the Biological Warfare Pathogen *Brucella Melitensis*. *J. Immunol. Methods* **2003**, *276*, 185–196.
43. Harstad, A. O.; Stipp, S. L. S. Calcite Dissolution: Effects of Trace Cations Naturally Present in Iceland Spar Calcites. *Geochim. Cosmochim. Acta* **2007**, *71*, 56–70.